Strain-rate-dependent compressive and compression-shear response of an alumina ceramic

Jie Zheng[a], Min Ji[a], Zahra Zaiemyekeh[a], Haoyang Li[a], James D. Hogan[a,*]

[a]*Department of Mechanical Engineering, University of Alberta, Edmonton, AB T6G 2R3, Canada.*

Abstract

This paper assessed the microstructure and properties of CeramTec ALOTEC 98 SB alumina ceramic through microscopic characterization and mechanical experiments. The rate-dependent strength and failure response of an alumina ceramics were studied under both uniaxial compression and compression-shear loading. Under quasi-static uniaxial compression at rates of 10^{-5} to 10^{3} s^{-1}, the strength had an average of 3393±306 MPa, and at dynamic strain rates of 10^{2} to 10^{3} s^{-1}, the strength ranged from 3763 to 4645 MPa. The CeramTec ALOTEC 98 SB alumina ceramic was found to have greater mechanical properties than other commercial alumina ceramics from the literature (i.e., AD-995). To monitor the strain field and the failure process of the alumina ceramic during testing, an ultra-high-speed camera coupled with digital image correlation (DIC) was used to visualize crack initiation and propagation processes, and obtain quantitative stress-strain information. A new data processing method was then proposed in this study to calculate the shear components for the compression-shear tests. Validation of the proposed method was confirmed by the shear strain obtained from the DIC analysis with the ultra-high-speed camera. Using the results obtained by the proposed model and the DIC analysis, new observations and understanding of failure mechanisms are obtained. 1) In compression-shear tests, the shear failure happens before complete failure, and shear behaviour plays an important role during the failure process. 2) The equivalent peak stress (strength) of compression-shear test is smaller than the uniaxial compression one. 3) The directional cracks have weak influence on the compressive stiffness, but have a strong influence on the shear response.

Keywords: Alumina ceramic, Microstructure, Strain-rate-dependent, Uniaxial compression, Compression-shear tests, Failure mechanisms

*Corresponding author
Email address: jdhogan@ualberta.ca (James D. Hogan)

1. Introduction

Advanced ceramics are used as critical structural components in applications of ballistic protection systems because of their superior hardness [1, 2, 3, 4] and strength-to-weight ratio [5]. During high velocity impact, ceramics experience different spatially- and temporally-evolving strain rates and stress states, resulting in various failure behaviors (e.g., brittle ceramics fracture and fragment in a conoidal volume) [5]. The effective application of advanced ceramics requires a thorough understanding of their mechanical response and failure behavior at various strain rates and stress states. To date, many efforts in studying the dynamic behavior of ceramics have been made for impact [6], tension [7, 8] and uniaxial compression loading [9, 10, 11, 12], with limited studies on the role of the shear component in dynamic failure under compression-shear loading [13]. This paper will explore both the compression and compression-shear response of an alumina ceramic.

Using a hydraulic confinement technique during compression experiments is one approach in the literature to study the shear-type response of brittle materials [14]. In their studies, Lankford et al. [15] and Anderson et al. [16] studied the dynamic compressive failure behaviour of silicon carbide at a strain rate of 1800 s^{-1} and confining pressures of 0 MPa to 200 MPa. In other studies, Hogan et al. [17] and Farbaniec et al. [18] investigated the dynamic fracture and fragmentation of boron carbide under biaxial confined compression. Their experimental results revealed the addition of confining pressure effectively suppresses unstable growth of the cracks and delays catastrophic failure. As an outcome of the suppression of failure, the shear strength is increased with increasing hydrostatic pressure, and the effect of strain rate on the strength of advanced ceramics diminishes with the confinement pressure increasing [14, 17]. However, in these experiments, limited efforts were applied to explore the influence of shear behaviour in the failure process [19, 20]. In the current study, we will explore the role of shear behaviour in the failure process under combined compression-shear loading.

Another way to obtain combined compression and shear loading is to use a modified split-Hopkinson Pressure Bar (SHPB) device or to utilize specimen with specially designed geometry structures, as is done in this paper. In their studies, Clifton [21], Baker and Yew [22], and Duff et al. [23] modified the conventional SHPB by adding a torsion device to achieve dynamic compression and shear loading. In related studies, Zheng et al. [24], Xu et al. [25] and Zhou et al. [26] used a compression-shear modified loading device to study rock materials, and Tan et al. [27] applied the same technique to study the dynamic failure of inorganic glass. All of these studies found that these materials exhibit obvious strain rate sensitivity and shear-dependency. Apart from modifying the SHPB device, changing the

shape of the specimen is another effective and implementable technique to generate shear stress in standard dynamic compression experiments. For example, Rittel et al. [28] and Zhao et al. [29] developed a special compression-shear specimen which is a cylinder with two diametrically opposed slots. As another example, Xu et al. [13] conducted both static and dynamic compression-shear experiments on rock materials through loading cuboid specimen containing parallel loading faces that are inclined to the loading direction. In their experiment, high-speed photographs were used to monitor the progressive failure process, and the results demonstrated that both shear-dominated failure and localized tensile damage appeared during the failure process, with the splitting failure mode being dominant. Different from confined compression experiments, in the compression-shear experiment of rock materials and glass, researchers [13, 24, 25, 26] concluded that the equivalent stress at failure decreases with an increasing shear portion in the stress, with obvious strain-rate effects noted. Despite numerous publications involving rocks in this area, the study of the shear-type behavior of advanced ceramics under compression-shear loading is less common, and this motivates the current study to address the gap in knowledge on the compression-shear behavior of the alumina ceramics.

This paper probed the microstructural characteristics and mechanical response of the material under strain rate dependent loading. First, microstructural characterization studies were carried out using scanning electron microscopy, energy-dispersive spectroscopy, Electron Backscatter Diffraction and X-Ray Microscopy. This characterization informs about the microscale features and chemical composition of the CeramTec ALOTEC 98 SB alumina ceramic under investigation here. Then, both uniaxial compression and compression-shear testing was carried out on a standard MTS machine at quasi-static strain rates ($10^{-5} \sim 10^{-3}s^{-1}$) and a split-Hopkinson pressure bar for dynamic strain rates ($10^{2} \sim 10^{3}s^{-1}$). To monitor the strain field and the failure process of the alumina, an ultra-high-speed digital camera was used in conjunction with digital image correlation (DIC) to visualize the crack initiation-propagation processes, and to obtain quantitative stress-strain information. A new data processing method was proposed in this study to calculate the shear strain and stress for the compression-shear tests, based on previous works in the literature [30, 31, 32] by now considering the evolution of Poisson's ratio and compressive stiffness induced by compressive loading. The validation of the proposed method was confirmed by the shear strain measured from the DIC analysis. The results show that the compression and shear responses of the alumina exhibit obvious strain-rate and stress-state dependent behavior. In the Discussion section, we compare mechanical properties of the CeramTec ALOTEC 98 SB alumina ceramic with other alumina from the literature [12, 33, 34, 35, 36,

37, 38, 39, 40]. We also discuss new observations of shear failure in ceramics made possible through the approaches pursued here. Overall, results from the present study provide a better understanding of the compression-shear failure behavior of alumina, including effects of strain rate and stress state, which is crucial in the design of next-generation protection materials.

2. Experimental methods

In this study, a commercially available alumina ALOTEC 98 SB from CeramTec (which is called CeramTec 98% in this paper), Germany, was studied. The number "98" refers to that the alumina content is approximately 98 mass percentage, with the remainder being sintering additives or trace impurities, and this is confirmed in microscopy analysis in section 4.1. The specimen was 2.3 mm by 2.7 mm in cross section and 3.5 mm in length, with tilting angles between parallel ends of 0° (for uniaxial compression tests) and 5° (for compression-shear tests). These sizes were chosen to give the material sufficient time to reach stress equilibrium to achieve more accurate results, as described in details in the literature [6, 12, 33, 41, 42, 43]. The shapes of specimens are shown in Figure 1. The cuboidal shape was chosen so that digital image correlation analysis could be performed on the flat surface of the specimen during the test, as well to better observe dynamic fracture behaviors. The surface of the specimens was sprayed with speckle patterns (with the paint spot size in the range of 20 to 30 μm) using a fine-tipped air brush to facilitate digital image correlation.

2.1. Material characterization

Scanning electron microscopy (SEM), Electron Backscatter Diffraction (EBSD), and energy-dispersive x-ray spectroscopy (EDS) were used to perform the microstructural characterization (such as grain size and defects) and determine the elemental composition on mechanically polished surfaces of the alumina (i.e., polished down to 0.25 um). A Field Emission SEM (Zeiss Sigma, Oberkochen, Baden-Württemberg, Germany) equipped with EBSD and EDS detectors were used to perform the microstructural and elemental analysis in this study. The electron high tension voltage was set at 20 kV with the working distances of approximately 8.5 mm and 13.5 mm for the EDS and EBSD detectors, respectively. The working distances were selected to compensate for the detecting angle of the detectors and to ensure sufficient signal strength. The EDS and EBSD map data were analyzed using the Oxford AZtec software. Mechanically polished samples were coated with 6 nm of carbon to enhance conductivity.

2.2. Quasi-static uniaxial compression and compression-shear tests

The quasi-static uniaxial compression and compression-shear tests were carried out using a standard servohydraulic MTS 810 machine. The description of this setup is detailed in previously published papers from the authors [6, 42]. In order to prevent the MTS loading platens from being indented by the alumina samples and fragments, polished tungsten carbide (WC) platens were placed in between the specimen and the loading platens. For uniaxial compression tests (the specimen with tilting angles of 0°), high pressure grease was applied between the surfaces of the WC platen and specimen to eliminate the frictional effect and allow for lateral motion [6, 42]. On the contrary, for the compression-shear tests, no grease was applied to induce tangential force by friction and to make sure no surface sliding occurs between the specimen and platens [13]. In the quasi-static tests, the specimens were compressed under the displacement control setting along the long dimension (3.5mm) at a constant rate in the range of 3.5×10^{-4} to 3.5×10^{-2} mm/s. The force history was recorded by a 100 kN load cell with a background noise of $\pm$ 1 N. The strain field of the specimen surface was obtained by digital image correlation (see section 2.4 for details), and the strain rates in the axial direction were measured to be in the range of 10^{-5} to 10^{-3} s^{-1} by taking the slope of the digital image correlation outputted strain history curves. The measured strain rate is an order lower than the setting value (10^{-4} to 10^{-2}), and this is due to the compliance of the loading frame [44].

2.3. Dynamic uniaxial compression and compression-shear tests

The dynamic uniaxial compression and compression-shear tests were conducted on a modified split-Hopkinson pressure bar (SHPB). The experimental system used in this study was the same as in Koch et al. [33] and Lo et al. [6]. The incident and transmitted bar were 1016 mm and 914 mm in length, respectively, with a diameter of 12.7mm. The bars were made of hardened C-350 maraging steel with a density of 8080 kg/m^3, an elastic modulus of 200 GPa, and longitudinal wave velocity of 4975 m/s. The yield strength of the bar was approximately 2.68 GPa which meets the requirements for testing ceramics [45, 46]. Impedance-matched Ti-6Al-4V titanium alloy jacketed tungsten carbide platens were used in the dynamic tests to protect the incident and transmitted bars from being indented by the hard ceramic samples and fragments [46]. In dynamic uniaxial compression tests, high pressure grease was applied between the protection platens and specimen to reduce friction and allow for free lateral expansion for specimen. Similar to the quasi-static tests, no grease was used in the dynamic compression-shear tests to induce tangential force by friction and to make sure no surface sliding

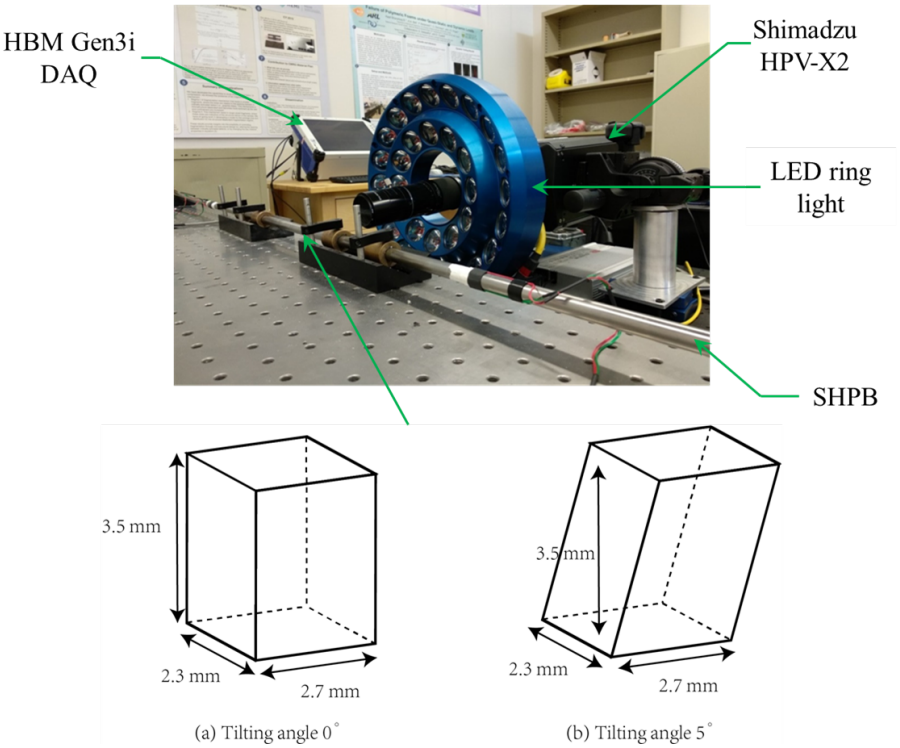

Figure 1: The split-Hopkinson pressure bar configuration for dynamic testing with an ultra-high-speed camera, a high-speed data acquisition system (DAQ) and an ultra-bright LED ring light. The insert below shows the geometries of the specimen: (a) uniaxial compression specimen with a tilting angle of 0°, and (b) compression-shear specimen with a tilting angle of 5°.

occurs between the specimen and loading devices [13]. The theory of the SHPB system has been well documented by Song and Chen [31], and the nominal axial stress of the specimen is computed using the strain gauge signal from the transmitted bar and the transmitted bar properties.

An HBM Gen3i High-Speed Recorder was employed for the data acquisition at 4 MHz with a Bessel IIR pre-filter to eliminate low frequency noise. In the current experiments, different types of pulse shaping configurations were used to produce near triangular pulses (i.e., tin and high density polyethylene (HDPE)), which is desired in testing linear elastic brittle materials [6]. The pulse shapers reduce the oscillation of the stress pulse due to dispersion effects and ensure the required stress equilibrium is achieved, as recommended in literature [6, 33, 47]. In order to achieve dynamic strain rates ranging from 80 to 850 s^{-1}, we varied the striker length (125 and 304 mm), as well as the types and dimensions of pulse shapers (tin, thin HDPE and thick HDPE), which are summarized in Table 1. Figure 2 and

Figure 3 show that the pulse shaping configurations used in the current study can induce uniform deformation across the sample surface and achieve near constant strain rates for the specimens, as is recommended in literature [6]. In all configurations of the setup, the 1-wave passage criterion was verified by comparing the rise time in the incident and transmitted pulses. More details of Figure 2 and Figure 3 are discussed next in section 2.4.

Table 1: Pulse shaping configurations used in dynamic experiments

Strain Rate (s^{-1})	Pulse Shaper			Striker Length (mm)
	Material	Diameter (mm)	Thickness (mm)	
80 to 150	Tin	3.97	1.59	304
300 to 450	HDPE (thin HDPE)	3.18	1.59	304
500 to 850	HDPE (thick HDPE)	3.18	2.38	125

2.4. Digital image correlation

In order to provide visualization on the specimen surface to monitor the macroscopic deformation, an AOS PROMON U750 high speed camera with a full resolution of 1280 × 1024 pixels recording at 5 to 500 frames per second (FPS, and its value is determined by the loading rate) was used in quasi-static tests, and an ultra-high-speed camera (Shimadzu HPV-X2) was used in dynamic tests. The Shimadzu HPV-X2 camera has a full resolution of 400 × 250 pixels, and the frame rates used in the tests ranges from 0.5 million to 5 million FPS depending on the pulse shaping configurations used (i.e., affecting the strain rates). An REL Inc. ultra-bright LED ring light was applied to provide sufficient lighting that enhanced imaging and DIC analysis. The exposure time was set at the range of 200 to 500 ns according to the frame rate of the camera and compensation for the lighting.

The DIC technique was applied to obtain the two-dimensional strain information and the failure process of the quasi-static and dynamic experiments by using the VIC-2D V6 software (Correlated Solutions, Inc. USA). During analysis, the surface of the specimen was discretized with a subset size of 31 × 31 pixels, and a step size of 7 pixels was chosen [6]. The zero-normalized sum of squared differences (ZNSSD) criterion with the optimized 8 tap interpolation scheme was utilized in the analysis.

In this study, the engineering strain was computed by DIC analysis, and the slope of the linear portions of the strain-time curves was taken as the strain rate. Figure 2 and Figure 3 show the

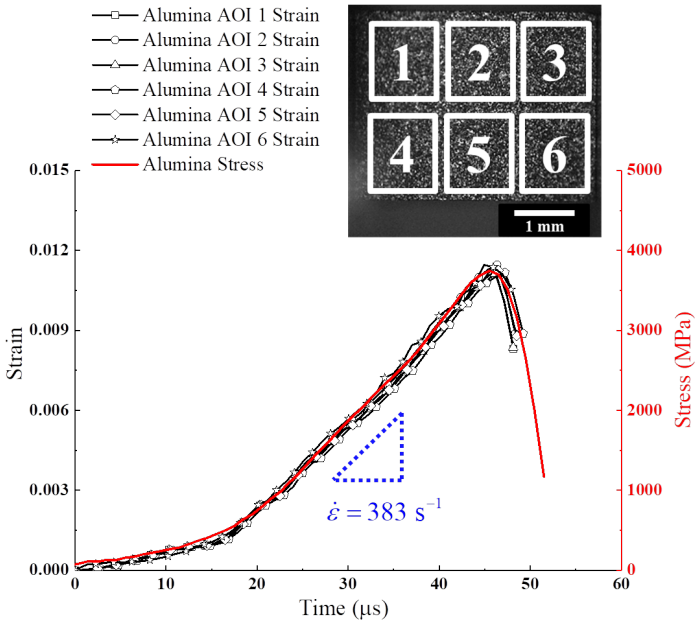

Figure 2: For specimen under dynamic uniaxial compression, the stress profile obtained from the transmitted gauge and the local strain profiles computed from six different areas of interest (AOI) by DIC are matched in time. The locations of the six AOIs are shown in the inset. The linear portions of the strain-time curves is taken as the strain rate, and the average strain rate in this experiment is approximately 383 s^{-1}.

representative stress and strain history for the dynamic uniaxial compression and compression-shear tests on the CeramTec 98% alumina, respectively. Six different local areas of interests (AOI) for strain-time are plotted with the stress-time to verify the stress equilibrium of the tests. It is observed that all six strain-time profiles are overlapped with each other, and this indicates that the specimen was deformed uniformly during loading [31]. In addition, the strain profiles were matched well with the stress history curve, which is expected for a typical linear elastic brittle material, and further demonstrates stress equilibrium during loading [6]. Lastly, the stress-strain curves were obtained by matching the average strain profile with the stress profile generated from the quasi-static and dynamic experiments. The average strain was calculated by averaging across the entire specimen surface.

3. Data processing method for combined compression and shear loading

In this section, we propose a new method that includes the force and deformation analysis during the compression-shear tests used to calculate the shear strain and stress based on previous work

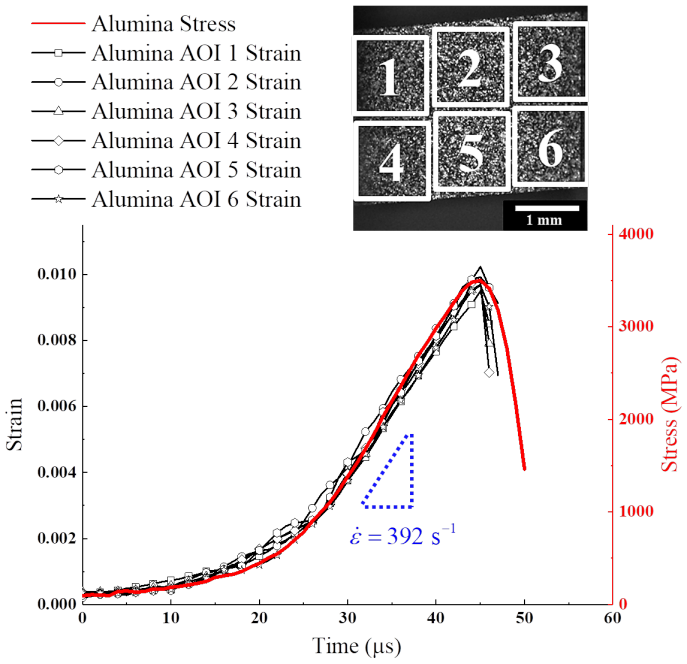

Figure 3: For specimen under combined dynamic compression and shearing loading, the axial stress profile obtained from the transmitted gauge and the local axial strain profiles computed from six different areas of interest (AOI) by DIC are matched in time. The locations of the six AOIs are shown in the inset. The linear portions of the strain-time curves is taken as the axial strain rate, and the average strain rate in this experiment is approximately 392 s^{-1}. The axial direction is the horizontal direction.

[30, 31]. This new method considers: 1) the evolution of Poisson's ratio induced by the loading [48, 49] and 2) the damage evolution of the compressive stiffness [48, 50]. The degrees of changes in these elastic properties depends on the material [49]. This proposed method is validated with the DIC measurements in the current study, which will be shown later.

As reference for this analysis, labeled in Figure 4a, F_n and F_t are the normal force and the tangential force applied on the specimen, respectively, where the tangential force is induced by friction. In Figure 4b, α is the tilting angle of 5°, γ and θ are the shear strain, d is the loading displacement, and h is the length of the specimen. In compression-shear testing, it is difficult to measure the tangential force directly, and so the current study proposes a data processing method to calculate the tangential strain and stress. To do this, our study utilized existing literature [31] to develop some assumptions to calculate the tangential force: 1) there is no surface sliding between the loading device and specimen

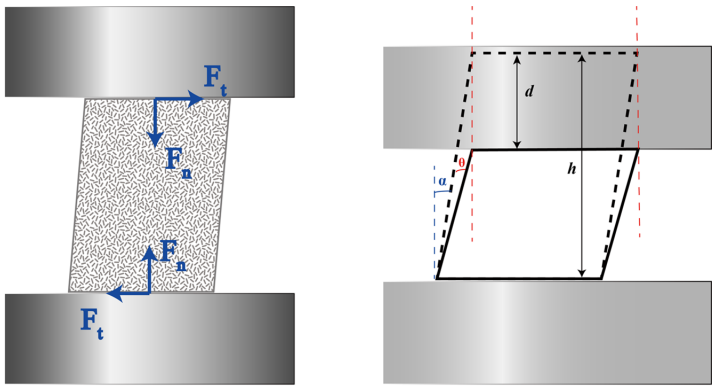

Figure 4: The analysis of force and deformation of the specimen during compression-shear testing: (a) the force analysis of the specimen, where the specimen is sprayed with a speckle pattern for digital image correlation which allows for measurements of compression and shear strains. F_n and F_t are the normal force and the tangential force applied on the specimen, respectively, where the tangential force is induced by friction. (b) the deformation analysis of the specimen with the assumption that no surface sliding happens, as indicated by the red dashed lines. The black dashed lines demonstrate the initial location of the specimen, and the solid line is the specimen under compression and shear loads. α is the tilting angle of 5°, θ is the shear strain, d is the loading displacement, and h is the length of the specimen.

(i.e., no grease applied between specimen and platen surfaces), as the red dashed line in Figure 4b shows, and 2) when the specimen reaches the equilibrium state, the deformation is uniform, and the strain and stress can be determined. Also, it is emphasized that these assumptions are consistent with the observation from images of the ultra-high-speed camera acquired in this study.

When no surface sliding occurs between the specimen and loading devices, and the value of d is extremely small, the normal strain ϵ, the shear strain γ and their incremental form can be expressed as:

$$\varepsilon = \frac{d}{h}, \quad \Delta\varepsilon = \frac{\Delta d}{h} \tag{1}$$

$$\gamma = \theta \approx \frac{d}{h-d}\tan\alpha \approx \frac{d}{h}\tan\alpha, \quad \Delta\gamma \approx \frac{\Delta d}{h}\tan\alpha \tag{2}$$

In a general case, the non-linear constitutive relationship of the alumina is:

$$\Delta\sigma = \frac{E(1-v)}{(1+v)(1-2v)}\cdot\Delta\varepsilon_1 + \frac{E\cdot v}{(1+v)(1-2v)}\cdot(\Delta\varepsilon_2+\Delta\varepsilon_3) \approx \frac{E(1-v)}{(1+v)(1-2v)}\cdot\Delta\varepsilon \tag{3}$$

$$\Delta\tau = G \cdot \Delta\gamma \tag{4}$$

where $E = E(\sigma)$ is the elastic modulus, $G = G(\sigma)$ is the shear modulus, and $v = v(\sigma)$ is the Poisson's ratio. Based on the study of Koch et al.[43, 48], E, G and v are regarded as functions of the stress, and their relationship is:

$$G(\sigma) = \frac{E(\sigma)}{2[1 + v(\sigma)]} \tag{5}$$

The normal force and the tangential force follow:

$$F_{\mathrm{n}} = \sigma \cdot A_s, \quad F_{\mathrm{t}} = \tau \cdot A_s \tag{6}$$

where A_s is the cross sectional area of the specimen. As a result of the dependency of the elastic modulus, shear modulus and Poisson's ratio on the stress state and level, the relationship between the tangential and normal force in an incremental form is obtained by combining Equations (1) to (6):

$$\frac{\Delta F_t}{\Delta F_{\mathrm{n}}} = \frac{G(\sigma)}{E(\sigma)} \cdot \frac{(1+v)(1-2v)}{(1-v)} \tan\alpha = \frac{[1 - 2 \cdot v(\sigma)] \tan\alpha}{2 \cdot [1 - v(\sigma)]} \equiv \tan\beta \tag{7}$$

Here β is the effective frictional angle of the contact surface of the specimen with the loading devices, and it refers to the ratio of the normal component to the shear component of surface force applied on the specimen. Note here that β is different from tilting angle α.

According to Equation (6) and Equation (7), increments of compressive and shear stresses in the specimen satisfy:

$$\Delta\sigma = \frac{\Delta F_{\mathrm{n}}}{A_s} \tag{8}$$

$$\Delta\tau = \frac{\Delta F_{\mathrm{n}}}{A_s} \frac{\left[1 - 2 \cdot v(\sigma)\right] \tan\alpha}{2 \cdot \left[1 - v(\sigma)\right]} \tag{9}$$

According to Equation (7), the compression and shear force can be obtained by the strain signals measured on the transmitted bar in an incremental form:

$$\Delta F_{\mathrm{n}} = A_b \cdot E_b \cdot \Delta\varepsilon_t(t) \tag{10}$$

$$\Delta F_t = A_b \cdot E_b \cdot \frac{\left[1 - 2 \cdot v(\sigma)\right] \tan\alpha}{2 \cdot \left[1 - v(\sigma)\right]} \cdot \Delta\varepsilon_t(t) \tag{11}$$

where t is the time, A_b and E_b are cross-sectional areas and elastic modulus of the impact bar and the support bar, respectively, and ε_t is the strain signals of the transmitted wave recorded by the strain gauges.

The relative loading displacement d in Figure 4b can be determined by DIC analysis, and thus d and its increment are:

$$\Delta d(t) = h \cdot \Delta\varepsilon = h \cdot \Delta\varepsilon(\Delta\varepsilon_0, D_{E_c}) \tag{12}$$

$$d(t) = h \cdot \int_0^t \left[\Delta\varepsilon(\Delta\varepsilon_0, D_{E_c})\right] dt \tag{13}$$

where ε is the axial strain obtained from DIC analysis, D_{E_c} is the damage to the compression stiffness, and ε_0 is the axial strain without any damage. Similarly, according to Equations (1) and (2), the compressive strain and shear strain in incremental form are expressed as:

$$\Delta\varepsilon(t) = \Delta\varepsilon(\Delta\varepsilon_0, D_{E_c}) = \Delta\varepsilon \tag{14}$$

$$\Delta\gamma(t) = \tan\alpha \cdot \Delta\varepsilon(\Delta\varepsilon_0, D_{E_c}) = \tan\alpha \cdot \Delta\varepsilon(t) \tag{15}$$

In order to compare the uniaxial compression results and the compression-shear results across the range of strain rates probed here, the equivalent stress and equivalent strain rate are used. The equivalent stress is expressed as:

$$\sigma_e = \sqrt{\frac{1}{2}\left[\left(\sigma_x - \sigma_y\right)^2 + \left(\sigma_x - \sigma_z\right)^2 + \left(\sigma_y - \sigma_z\right)^2 + 6\left({\tau_{xy}}^2 + {\tau_{xz}}^2 + {\tau_{yz}}^2\right)\right]} \tag{16}$$

The equivalent strain rate is analogous to the equivalent stress and is expressed as:

$$\dot{\varepsilon}_e = \sqrt{\frac{1}{2(1+v)^2}\left[\left(\dot{\varepsilon}_x - \dot{\varepsilon}_y\right)^2 + \left(\dot{\varepsilon}_x - \dot{\varepsilon}_z\right)^2 + \left(\dot{\varepsilon}_y - \dot{\varepsilon}_z\right)^2 + 6\left(\dot{\varepsilon}_{xy}^2 + \dot{\varepsilon}_{xz}^2 + \dot{\varepsilon}_{yz}^2\right)\right]} \tag{17}$$

4. Experimental results

4.1. Material characterization

The microstructural features of the CeramTec 98% alumina were first investigated by examining the intact material surface. Figure 5a is an SEM micrograph showing a typical microstructure of the

CeramTec 98% alumina. The grey regions correspond to the alumina phase, and the surface pores can be observed. Some of the porous features in Figure 5a are secondary glassy phases that were removed during mechanical polishing [33], confirmed by EDS analysis (shown later). Figure 5b shows an EBSD map for the CeramTec 98% alumina, and it shows the grain size and the crystal orientation of the grains at the surface of the sample. Based on the Figure 5b, the equivalent circle diameters of grains were determined by using the AZtec Channel 5 software, with an average of $1.85 \pm 0.98 \mu$m. Specifically, the large standard deviation is associated with the large horizontal high-aspect-ratio grains. Figure 6 shows approximately 88% of the grain size (the equivalent circle diameters) distribution is between 0.4 and 2.8 μm, and they are nearly circular small grains. There are also a relatively small number of large horizontal high-aspect-ratio grains with the equivalent circle diameters ranging from 5 to 8 μm. Next, both small equiaxed and large columnar grains appear to have no preferred crystallographic orientation, and most boundaries are of high misorientation angle (>15°). The large grains with higher aspect ratios appear to be more-or-less aligned near-parallel with each other. Lastly, the unindexed (black) regions in Figure 5b are believed to be corresponding to either the pores or regions with impurities. Those impurities can easily form a glassy phase concentrated at the grain boundaries [33, 51], and the impurity analysis has been conducted using the EDS data (shown later).

The X-Ray Microscopy (XRM) was also applied to characterize the defects (pores and impurities) in the sample. XRM scans of the samples were carried out using a ZEISS Xradia Versa 620, with X-ray voltage 100 kV, power 14.02 W and a voxel size of $0.5275 \times 0.5275 \times 0.5275$ μm^3. Only the central volume of the sample (a cylinder with a height of 0.61 mm and a diameter of 0.53 mm) was considered for XRM analysis, as Figure 7a and b shows. The Dragonfly Pro software (Object Research Systems, Inc. Canada) was used to explore the data, and the reconstructed pores were filtered by a minimum of 8 voxels (a resolution limit consistent with those used in the literature [34, 52]). The histogram distribution of different defect volumes is shown in Figure 7c, and most of the defects are less than 160 μm^3 in volume. The largest volume of the defect is around 10200 μm^3 and large defects are infrequent in the sample. The volume percentage of the defects is around 1%.

Next, the elemental composition and impurity distribution are examined using EDS. Figure 8 and Table 2 show the elemental composition of the CeramTec 98% alumina determined in terms of weight percentage and atomic percentage by EDS. This material is primarily composed of aluminum (atomic 39.52%, weight 52.47%) and oxygen (atomic 59.47%, weight 46.1%) mixed with traces of Mg (atomic 0.49%, weight 0.58%), Si (atomic 0.27%, weight 0.37%), and Ca (atomic 0.25%, weight 0.48%). Carbon

is excluded from the concentration calculation since it is likely introduced during sample preparation (mechanical polished with liquid-suspended diamond and carbon coating to enhance conductivity). For pure alumina, the ratios of atomic percentage of aluminum to oxygen should be 2:3, and an excess of oxygen element would indicate oxide contaminants. The distribution of magnesium, calcium and silicon may come from manufacturing process [53]. Overall, the material is confirmed to be single phase α-alumina verified by SEM and EDS.

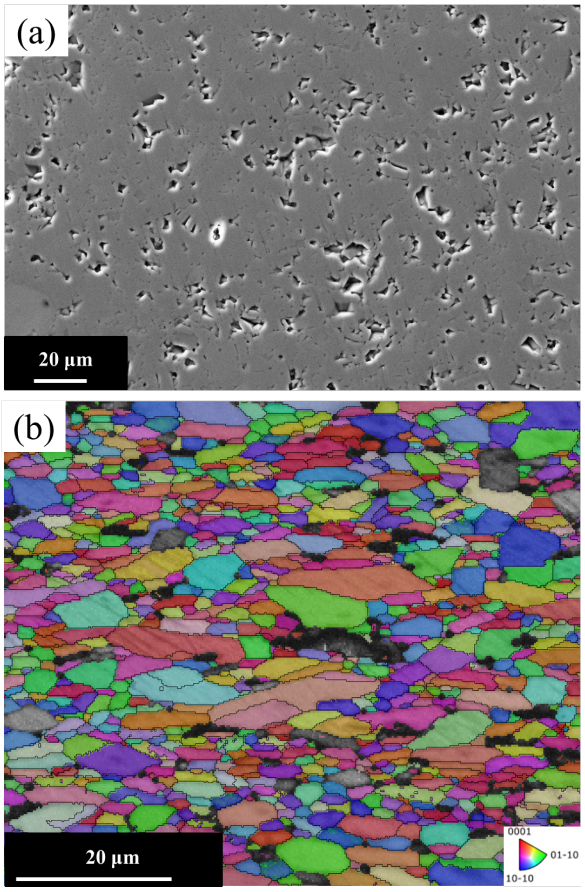

Figure 5: (a) SEM image of a polished alumina surface which shows the micro-structural features of the alumina. The grey regions correspond to the alumina, and the surface pores can be observed. (b) EBSD maps for the CeramTec 98% alumina, and this map shows the grain size and the crystal orientation of the grains at the surface of the sample.

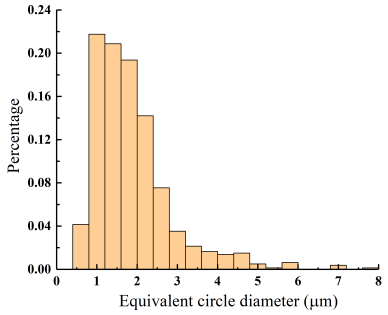

Figure 6: The histogram distribution of the equivalent circle diameter of the grain in the CeramTec 98% alumina, which is obtained from several regions of the sample. Approximately 88% of the grain size (the equivalent circle diameters) distribution is between 0.4 and 2.8 μm, and they are nearly circular small grains. There are also a relatively small number of large horizontal high-aspect-ratio grains with the equivalent circle diameters ranging from 5 to 8 μm..

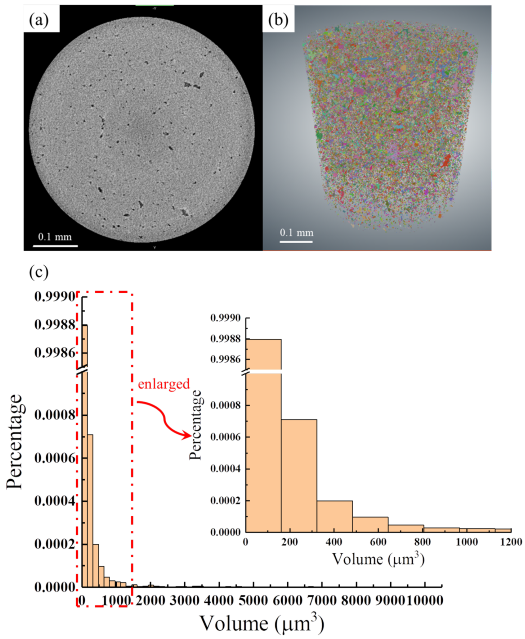

Figure 7: (a) and (b): The central volume of the sample, a cylinder with a height of 0.61 mm and a diameter of 0.53 mm, was considered for the XRM analysis. The colored volumes in (b) are the defects (pores and impurities) in the sample. (c) The histogram of defects with different size volumes. The volume value of the defects is dominated by small ones (less than 160 μm^3), and large defects are infrequent (the largest volume of the defect is around 10200 μm^3). The histogram of the volumes less than 1200 μm^3 is enlarged in the inset.

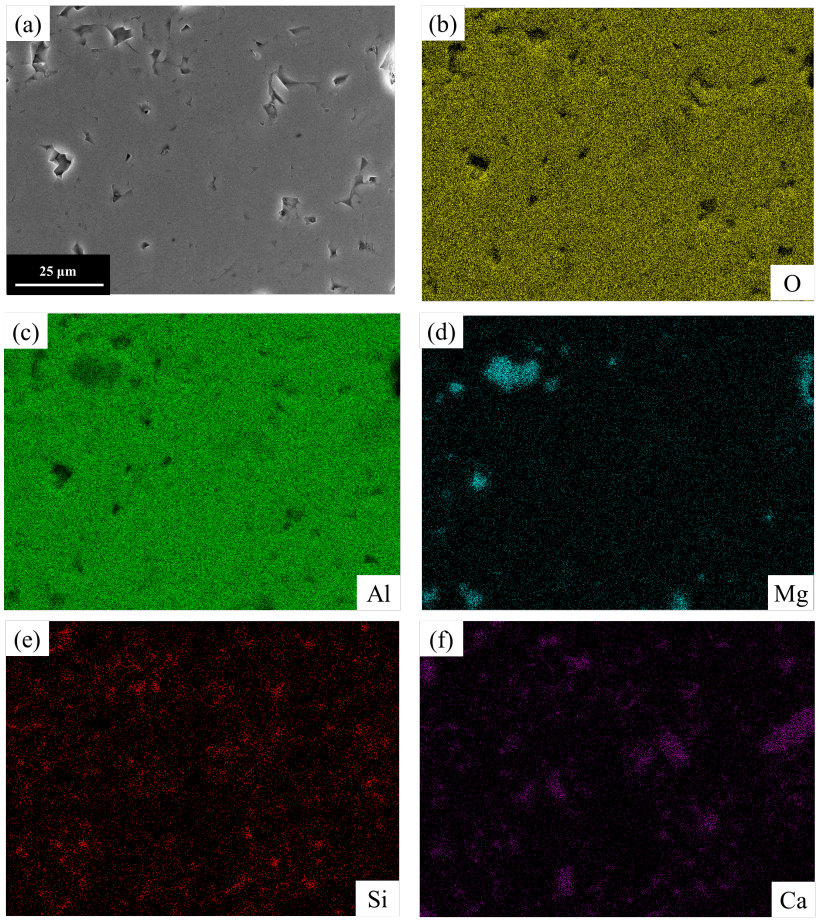

Figure 8: SEM coupled with EDS investigating the chemical composition of the alumina. (a) SEM micrograph showing a magnified view of a mechanically polished surface of the CeramTec 98% alumina. (b) EDS map of the distribution of oxygen. (c) EDS map of the distribution of aluminum. (d) EDS maps of magnesium element. (e) EDS maps of silicon element. and (f) EDS maps of the calcium element. The magnesium, silicon and calcium elements are present in low quantities.

Table 2: Elemental composition of the CeramTec 98% alumina as determined by EDS

Element	Weight (%)	Atomic (%)
O	46.1	59.47
Al	52.47	39.52
Mg	0.58	0.49
Si	0.37	0.27
Ca	0.48	0.25

4.2. Strain-rate dependent uniaxial compression tests

In the current study, four quasi-static tests with strain rates ranging from 1.6×10^{-5} to 1.63×10^{-3} s^{-1} and eleven dynamic tests with the strain rates ranged from 83 to 835 s^{-1} were performed for the alumina under uniaxial compression. Figure 9 shows the representative stress-strain curves where the solid lines represent the uniaxial compression tests. The stress-strain curves are shown as nearly-straight lines. When the stress-strain curves reach the peak value, the specimen failed catastrophically, and the stress drops immediately in both quasi-static and dynamic tests. The Young's modulus and Poisson's ratio remain near-constant before failure, as Figure 9 and Figure 10 show, and their values are calculated by taking the slope of the stress-strain curve and the lateral-axial strain curve, respectively. Under the quasi-static condition, the Young's modulus has an average of 356 ± 28 GPa, and an average of 380 ± 42 GPa under the dynamic condition. Similarly, the Poisson's ratio has an average of 0.243 ± 0.023 under the quasi-static condition, and 0.226 ± 0.030 under the dynamic condition. A summary of the data is shown in Table 3. These properties are consistent with the reported values of alumina ceramics [33].

Figure 11 shows the relationship of the compressive strength and the strain rate for the CeramTec 98% alumina. From Equation (16) and Equation (17), the equivalent peak stress and corresponding strain are computed, and their values are also listed in Table 3 for clarity. It is observed that the CeramTec 98% alumina shows rate dependence in its compressive strength. For the quasi-static experiments at the strain rates of 1.6×10^{-5} to 1.63×10^{-3} s^{-1}, the compressive strength has an average of 3393 ± 306 MPa, and the failure strain was $0.88\pm0.11\%$. For the dynamic experiments at strain rates of 83 to 835 s^{-1}, the compressive strength has an average of 4126 ± 297 MPa (with an average of 4126 MPa) and the failure strain was $1.13\pm0.17\%$. In the current study, the CeramTec 98% alumina

has approximately a 22% increase in strength across the studied strain rates, and these results are consistent with the recent SHPB results by Koch et al. [33] on the CoorsTek AD-85 (around 30% increase) and AD-995 (around 50% increase) alumina ceramics (see section 5.1 for details).

4.3. Strain-rate dependent compression-shear tests

In the current study, six quasi-static compression-shear tests with axial strain rates ranging from 1.5×10^{-5} to 1.6×10^{-3} s^{-1} and nine dynamic compression-shear tests with axial strain rates ranging from 82 to 833 s^{-1} were performed for the alumina. Similar to uniaxial compression results, the axial stress and axial strain curves for the compression-shear tests are shown as nearly-straight dash lines in Figure 9 with little softening occurring prior to failure, which corresponds to D_{E_c} in Equation (14) in our proposed model. The Young's modulus and Poisson's ratio in the compression-shear tests are in the same range as the uniaxial compression tests, as the dash lines in Figure 9 and Figure 10 show. As before, Table 3 lists the data. In order to compare the uniaxial compression and the compression-shear results, the equivalent stress (Equation (16)) and equivalent strain rate (Equation (17)) are used. Figure 11 and Table 3 show the equivalent peak stress and the equivalent strain rate of both uniaxial compression and compression-shear tests. It is observed that the equivalent peak stress of the compression-shear tests is smaller than the uniaxial compression one. The significance of these results will be discussed later.

Next, to validate the proposed model in section 3 and better understand the role of shear failure on the mechanical response in compression-shear tests, the predicted shear strain calculated by using Equation (15) is compared with shear strain obtained by DIC analysis in Figure 12. It is notable in Figure 12 that the peak value in the black DIC curve occurs sooner in time than that of the red predicted curve. The red curve in Figure 12 is derived from Equation (15): $\Delta\gamma(t) = \tan\alpha \cdot \Delta\varepsilon(t)$, whose time is related to the complete failure of the sample. It means the shear failure happens earlier than complete failure. There are also minor differences in time-evolved magnitudes between the DIC results and the model results, which may be induced by different crack and damage evolution, which are themselves strain-rate dependent. More specifically, in quasi-static loading, fewer defects are activated and the evolution of the cracking is considered less interacting [49]. In dynamic loading, multi-cracks are nucleated and grow. As the strain rate is further increased, the density of cracking nucleation increases, and these cracks will interact and coalesce with each other [49]. These rate effects in terms of nucleation, growth, interaction, and coalescence results in differences in damage

accumulation behaviors. Altogether, the validation from Figure 12 shows the predicted model is in reasonable agreement with the experimental results.

Finally, the time-evolution of surface fracturing is investigated by relating high-speed images acquired during dynamic experiments with stress-time information. In both uniaxial compression and compression-shear tests, the surface cracks are primarily directional cracks in the axial direction (almost parallel to the lateral edge), as Figure 13 and Figure 14 show.

5. Discussion

5.1. Microstructure and mechanical properties of comparable alumina ceramics

In this study, the chemical composition, microstructure and mechanical characterization of the CeramTec 98% alumina ceramic have been investigated. In this sub-section, a comparison is made between the CeramTec 98% alumina, the CoorsTek alumina ceramics (AD-85 and AD-995) and others from the literature [12, 33, 34, 35, 36, 37, 38, 39]. Comparing microstructures among this study and the CoorsTek alumina, it is found that the CeramTec 98% alumina has fewer intergranular defects (the defect volume fraction is around 1%), which is similar to AD-995 (the defect volume fraction is around 1%) but much fewer than AD-85 (the defect volume fraction is around 4%) [33, 34]. Additional previous studies on AD-995 by Lankford et al. [36] demonstrated the AD-995 material has larger and more porosity than the CeramTec 98%, although this conclusion is made on limited available micrographs. In the CERAMSHIELD CAP3 material in Swab et al. [12], there is a greater number of intergranular phases and more frequent porosity features, although the authors do not necessarily quantify the amount or types of phases. These intergranular impurities and pores serve as crack nucleation sites [33], and so are detrimental to material performance. Further, the grain size of the CeramTec 98% alumina (over 88% is between 0.4 and 2.8 μm) is much smaller than that in Coorstek AD-995 (8 ± 3 μm) [33]. In the CERAMSHIELD CAP3 alumina in Swab et al. [12], the grain sizes measured using outlines of their intergranular phases in their SEM images yield sizes of 15.3$\pm$9.7 μm. These differences are notable because past studies [54, 55] have found ceramics with smaller grain sizes will have better mechanical performance.

To probe these comparisons further, a summary of the uniaxial compression strength of various alumina ceramics under strain rates of $10^{-5} \sim 2500s^{-1}$ [33, 34, 35, 36, 37, 38, 39, 40] is shown in Figure 15. Note that most commercial names are known, while some are not. Also, we are only

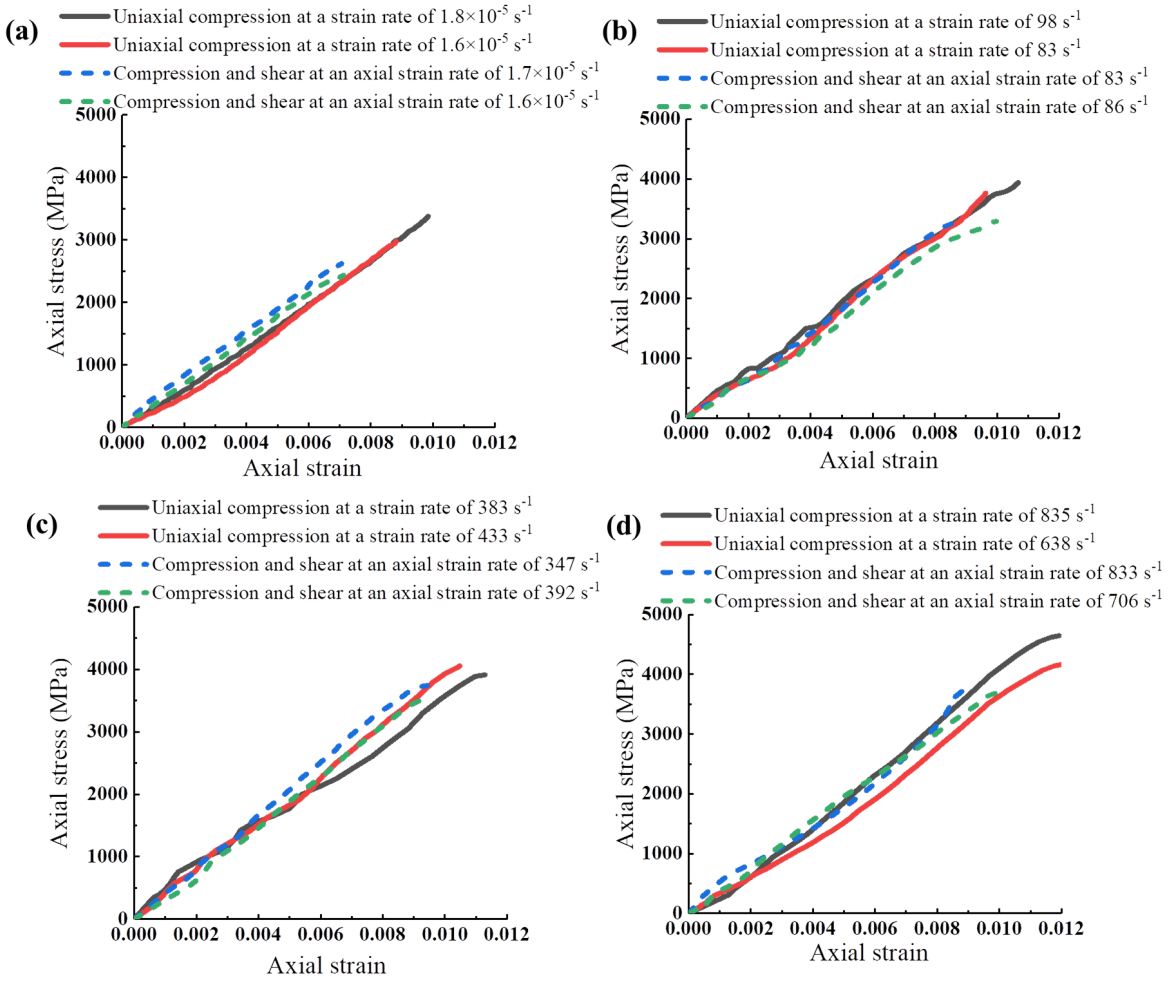

Figure 9: Representative stress-strain curves in the axial direction at quasi-static and dynamic strain rates (with three different pulse shaping configurations shown in Table 1) for the CeramTec 98% alumina. The solid lines correspond to the uniaxial compression tests, and the dashed lines correspond to the compression-shear tests. Additional summarized data is provided in Table 3.

Table 3: The mechanical properties and responses of the CeramTec 98% alumina

	Young's modulus (GPa)	Poisson's ratio	Axial strain rate (s^{-1})	Equivalent strain rate (s^{-1})	Axial peak stress (MPa)	Equivalent peak stress (MPa)
Uniaxial compression test	349	0.228	1.8×10^{-5}	1.8×10^{-5}	3378	3378
	321	0.257	1.6×10^{-5}	1.6×10^{-5}	2977	2977
	367	0.219	1.54×10^{-3}	1.54×10^{-3}	3691	3691
	388	0.266	1.63×10^{-3}	1.63×10^{-3}	3529	3529
	395	0.203	98	98	3937	3937
	421	0.288	83	83	3763	3763
	403	0.224	93	93	4128	4128
	342	0.261	87	87	3760	3760
	372	0.235	115	115	4074	4074
	311	0.190	383	383	3914	3914
	407	0.216	433	433	4054	4054
	384	0.189	355	355	4593	4593
	411	0.211	835	835	4645	4645
	311	0.226	638	638	4201	4201
	428	0.242	785	785	4318	4318
Compression-shear tests	358	0.230	1.7×10^{-5}	1.70×10^{-5}	2620	2624
	364	0.247	1.6×10^{-5}	1.60×10^{-5}	2433	2436
	367	0.196	1.5×10^{-5}	1.50×10^{-5}	2656	2660
	342	0.213	1.6×10^{-3}	1.60×10^{-3}	2927	2931
	376	0.23	1.6×10^{-3}	1.60×10^{-3}	2972	2976
	364	0.199	1.6×10^{-3}	1.60×10^{-3}	3090	3095
	407	0.198	83	83.2	3278	3283
	396	0.289	86	86.2	3289	3292
	429	0.287	82	82.1	3303	3306
	425	0.249	347	347.6	3743	3748
	405	0.207	392	392.8	3500	3505
	398	0.24	364	364.7	3565	3565
	342	0.216	833	834.6	3720	3725
	353	0.239	706	707.3	3708	3713
	428	0.224	508	508.9	3186	3191

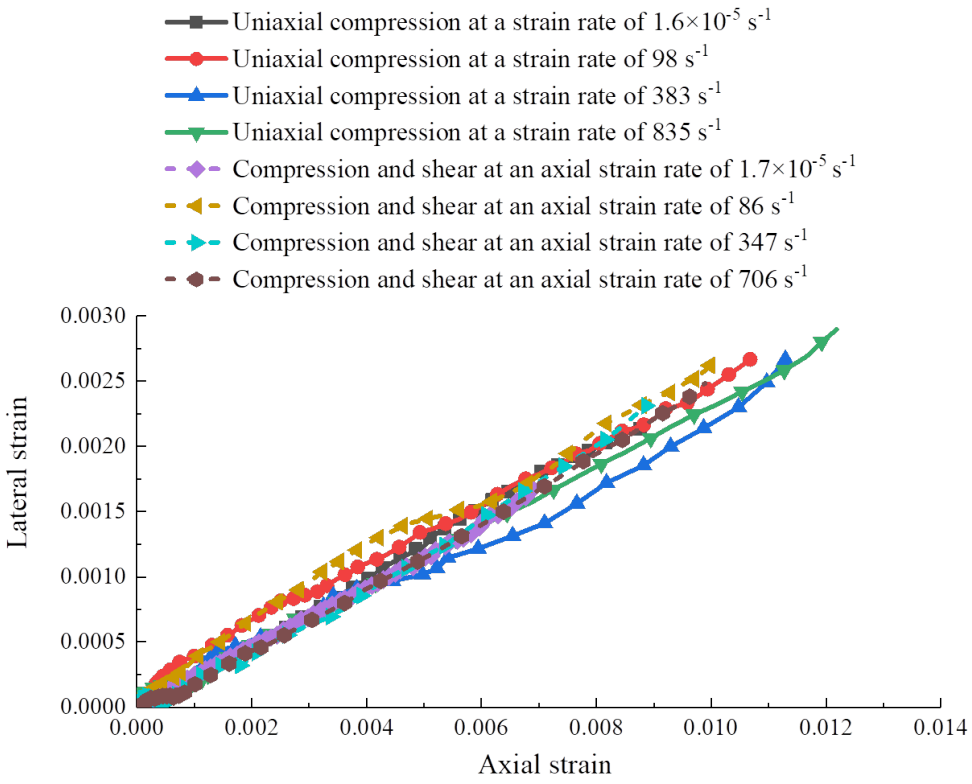

Figure 10: Representative lateral-axial strain curves at quasi-static and dynamic strain rates (with three different pulse shaping configurations shown in Table 1) for the CeramTec 98% alumina. The solid lines correspond to the uniaxial compression tests and the dashed lines correspond to the compression-shear tests, noting little differences between the two types of tests.

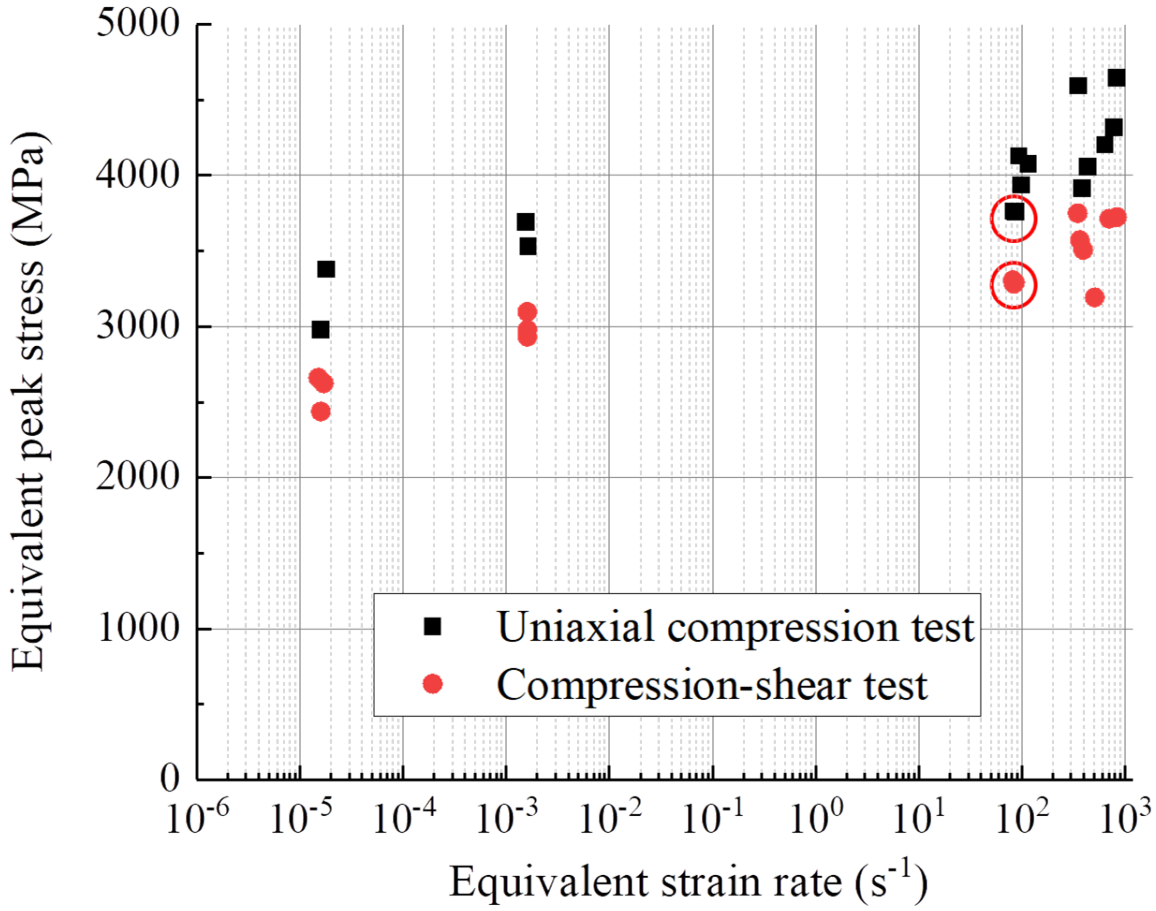

Figure 11: Semi-log plot of the equivalent peak stress and the equivalent strain rate for the CeramTec 98% alumina. The black rectangle points represent the uniaxial compression tests, and the red circle points represent the compression-shear tests. A black rectangle point in the figure is circled, because there are two points almost overlapped. A red circle point in the figure is circled, because there are three points almost overlapped.

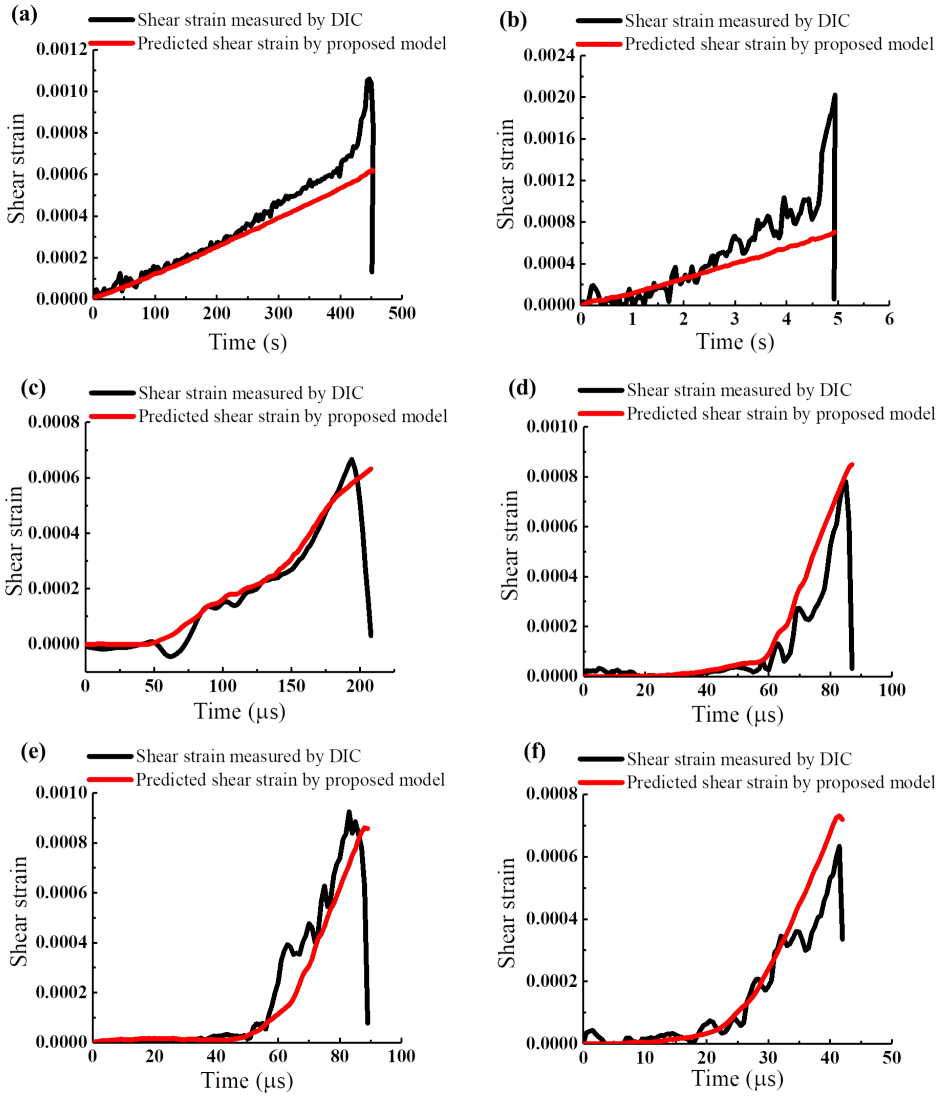

Figure 12: The shear strain-time curves from compression-shear tests at various strain rates. The black curves are the shear strain obtained from DIC analysis, and the red curves are the predicted shear strain by Equation (15): (a) shear strain-time curve at a quasi-static strain rate (1.6×10^{-5} s^{-1}), (b) shear strain-time curve at a quasi-static strain rate (1.6×10^{-3} s^{-1}), (c) shear strain-time curve at a strain rate of 83 s^{-1} (tin pulse shaper), (d) shear strain-time curve at a strain rate of 347 s^{-1} (thin HDPE pulse shaper), (e) shear strain-time curve at a strain rate of 392 s^{-1} (thin HDPE pulse shaper), and (f) shear strain-time curve at a strain rate of 706 s^{-1} (thick HDPE pulse shaper).

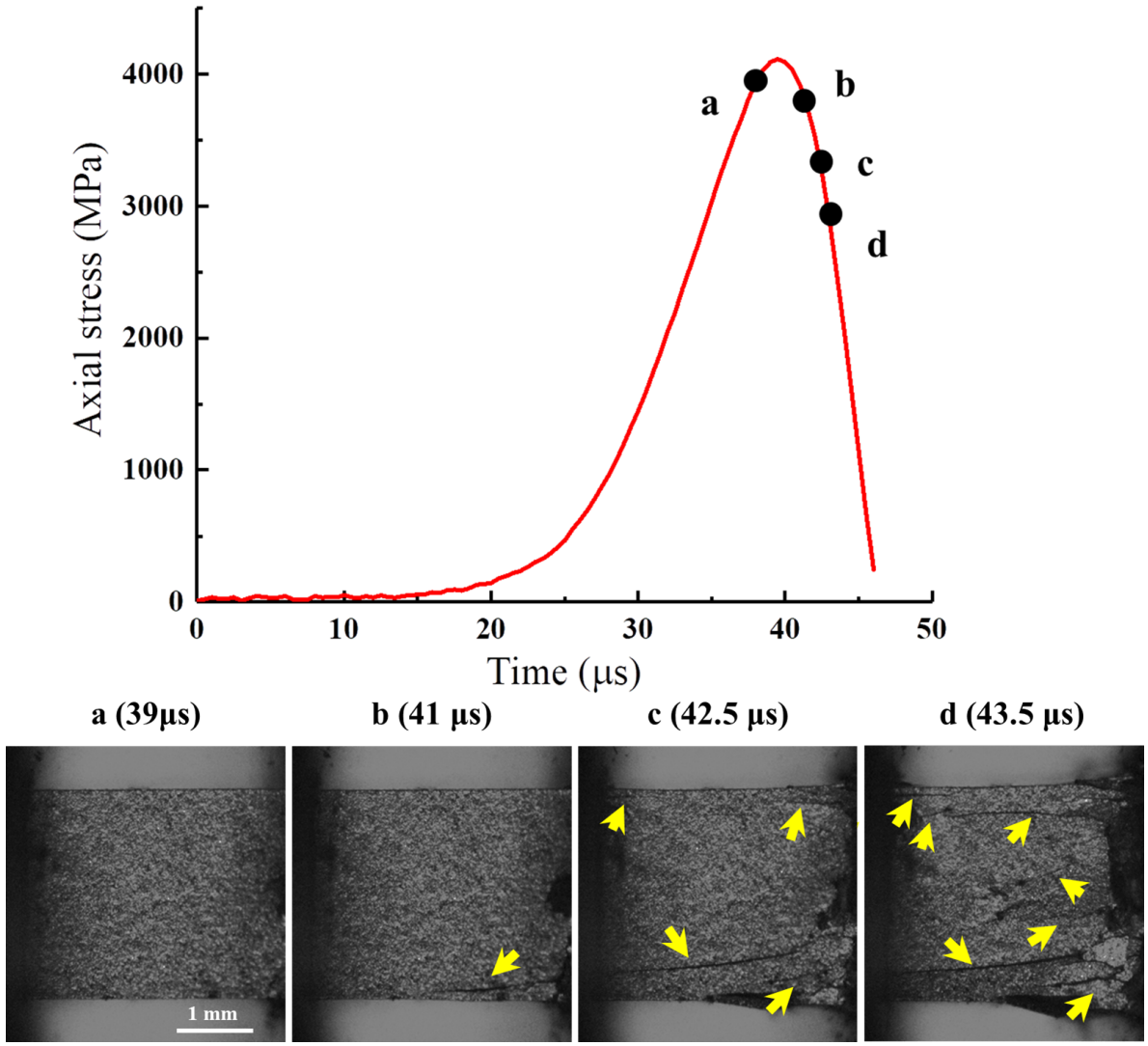

Figure 13: Time-resolved failure visualization for uniaxial compression test. The strain rate is around 638 s^{-1}. Ultra-high-speed photographs are shown in the inset, and their corresponding points are shown as the black points on the red stress-time curve. The cracks are pointed out by yellow arrows.

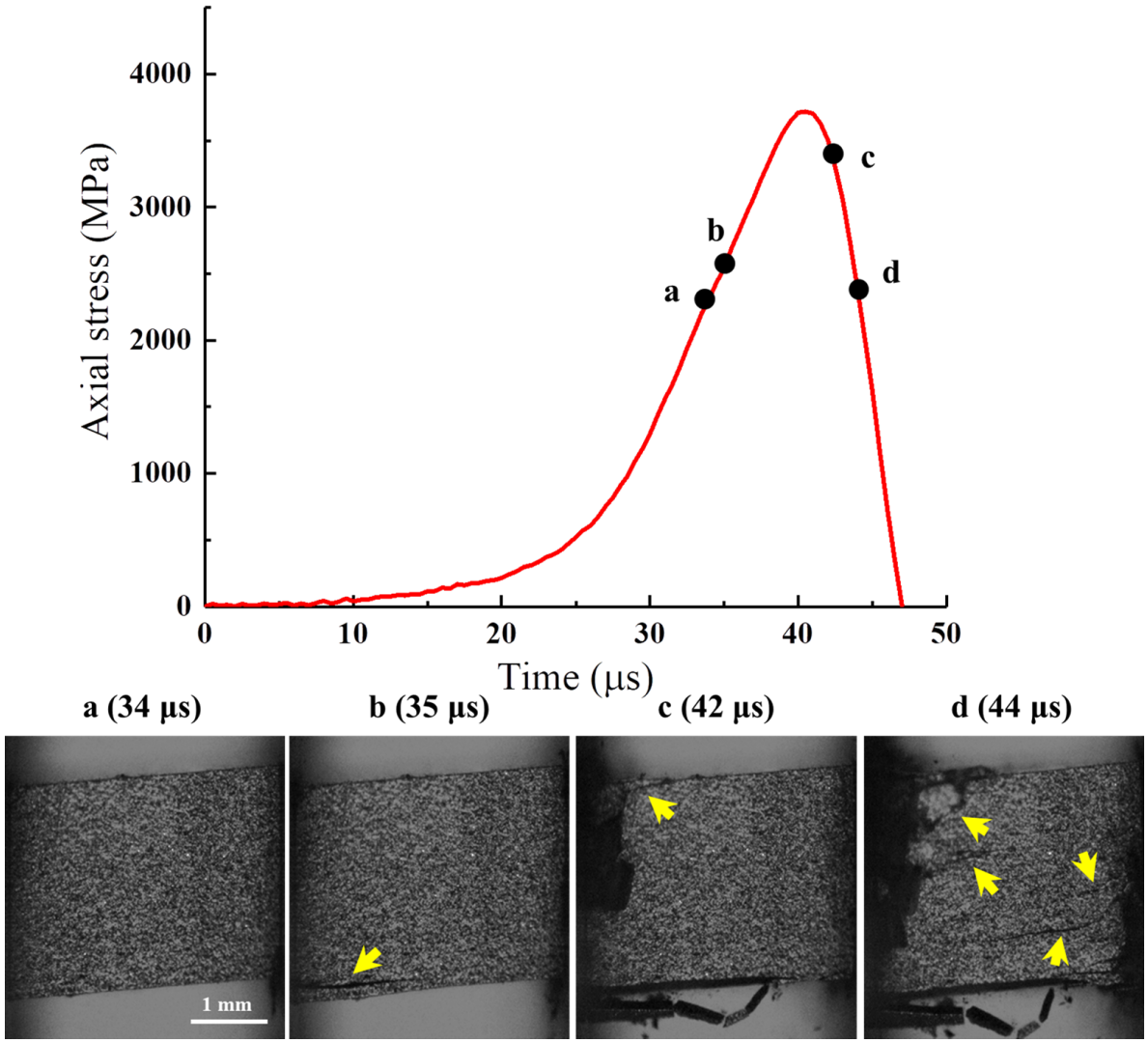

Figure 14: Time-resolved failure visualization for compression-shear test. The strain rate in the axial direction is around 706 s^{-1}. Ultra-high-speed photographs are shown in the inset, and their corresponding points are shown as the black points on the red stress-time curve. The cracks are pointed out by yellow arrows.

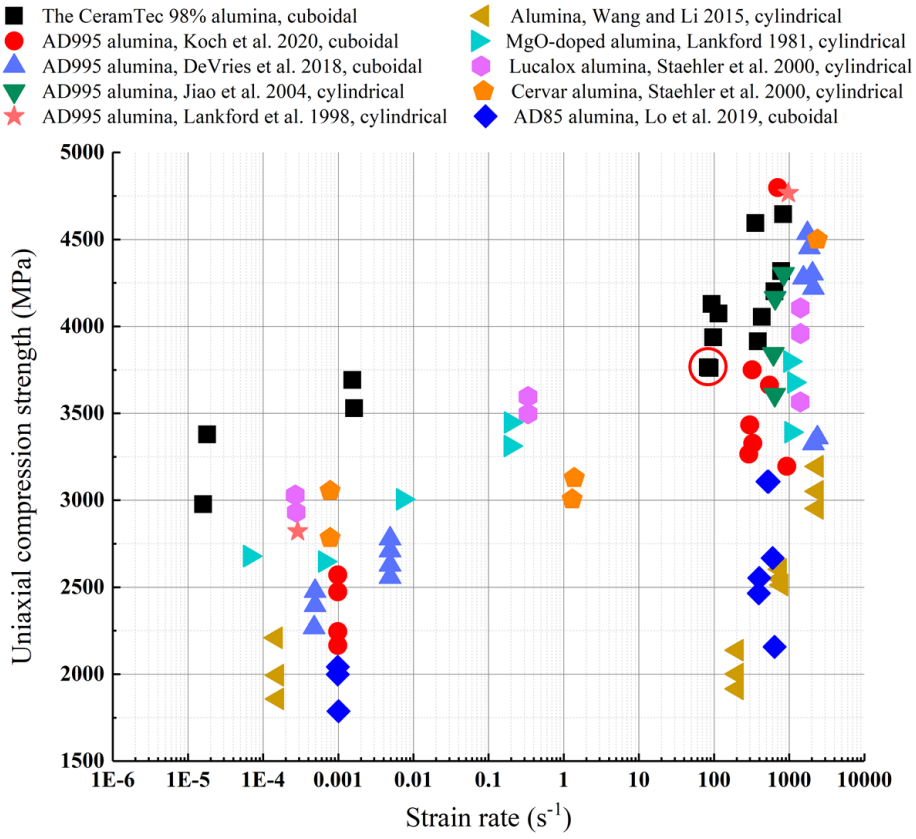

Figure 15: Summary of uniaxial compression strengths of various alumina ceramics with cylindrical or cuboidal shaped specimen. The black points are the uniaxial compression strength of the CeramTec 98% alumina from this study, and the other colored points are the uniaxial compression strength of other alumina obtained from literature [33, 34, 35, 36, 37, 38, 39, 40]. A black rectangle point in the figure is circled because there are two points almost overlapped.

making a comparison among test results acquired using cylindrical and cuboidal shaped specimen. In Swab et al. [12], dogbone specimen geometries were used and strength results are higher as described by those authors [33, 34, 35, 36, 37, 38, 39, 40], and we do not report their results in Figure 15. Here, we observe that the CeramTec 98% alumina has a greater quasi-static compressive strength (3393 ± 306 MPa), and generally greater dynamic strength, when compared with AD-995 (quasi-static strength of 2455 ± 366 MPa) [33, 35, 36, 40] and AD-85 (1942 ± 155 MPa) [33, 34]. From a survey of the limited literature involving Young's modulus measurements, the CeramTec 98% also has a higher experimentally measured Young's modulus (356 ± 28 GPa) when compared with AD-995 (elastic modulus of 303 ± 31 GPa [33, 36]) and AD-85 (elastic modulus of 221 ± 27 GPa [33, 34]). As highlighted earlier, these improvements in mechanical properties are likely related to the differences of defects and grain sizes [33, 34, 54, 55].

5.2. Shear-induced failure on mechanical response

In this final sub-section, we discuss the implications of the results in terms of acquiring a better understanding of the role of shear in failure of ceramics. We draw upon mechanical response (i.e., stress-strain response, strain-time curves and rate-dependent strength measurements) presented in the manuscript to articulate the importance of this study in modelling ceramic behavior, especially in impact applications [19, 20].

First, results presented in Figure 12 show that shear failure (peak shear strain) in the compression-shear experiments occurs sooner in time than complete failure, and the shear strain evolution is associated with rate effects manifested in shear strain. These rate effects and trends are believed to be related to localized nucleation, growth and interaction of the cracks [49] and crack sliding [56]. In quasi-static tests, the increase in shear strain is accelerated prior to failure (Figure 12a and b), indicating that $\dot{D} \rightarrow +\infty$ prior to catastrophic shear failure [49, 57, 58], where $\dot{D}$ is the damage in shear response. In this damage accumulation and failure process, compression-shear results from this study indicate that directional cracking has a stronger detrimental effect on the shear resistance of the material as indicated by shear strain evolutions (Figure 12a and b) when compared with the compressive resistance as indicated by the nearly linear stress-strain curve prior to peak strength (Figure 9a). Taken together, these results confirm that shear loading and associated shear damage accumulation play an important role in the failure process of brittle materials. The importance of shear has been noted previously in the literature for uniaxial compressive failure [33, 48, 59] and is a core assumption

in the wing crack model [56, 60, 61].The anisotropic damage evolution is an important consideration in failure modelling of brittle materials [49, 57, 58], where insights into stress-state dependent and non-linear damage forms can be gained from experimental results presented here.

Finally, a key observation from this paper is that the equivalent peak stress in combined compression-shear loading is smaller than that under uniaxial compression (Figure 11), which may related to the earlier shear failure (Figure 12) from overall increased damage accumulation and fracturing. As far as the authors are aware, this observation has not yet been made widely for ceramics, with most studies involving combined compression-shear loading occurring in rocks [13, 24, 26] and glass [27]. Based on the new results presented in this paper, it is important to consider stress-state dependent (e.g., combined or history-dependent loading) anisotropic damage accumulation evolution in models [49, 58, 62], and this will be of particular importance when simulating the response of advanced ceramics in impact and ballistic applications [6, 19, 20, 63, 64, 65, 66] where the materials experience spatially- and temporally-evolving combined stress states and strain rates.

6. Conclusion

This study assessed the performance of the CeramTec 98% alumina through microscopic characterization, and strain-rate-dependent uniaxial compression and compression-shear experiments. The microscopic characterization and mechanical performance of the CeramTec 98% alumina are compared with some other commercial alumina, and the CeramTec 98% alumina has higher mechanical properties stemming from Figure 15. A new data processing method was proposed in this study to calculate the shear components for the compression-shear tests. Validation of the proposed method was confirmed by the shear strain from the DIC analysis. By dealing with the results obtained by the proposed model and the DIC, new observation and understandings are made: 1) The shear failure happens before complete failure, and shear behaviour plays an important role during the failure process in compression-shear tests. 2) The equivalent peak stress (strength) of the compression-shear test is smaller than the uniaxial compression one. 3) The directional cracks have weak influence on the compressive stiffness, but have a strong influence on the shear behaviour.

7. CRediT authorship contribution statement

Jie Zheng: Conceptualization, Theoretical methodology, Experiment, Software, Investigation, Validation, Resources, Data curation, Writing – original draft, Writing – review editing, Visualization.

Min Ji: Experiment, Investigation, Validation, Writing – review.

Zahra Zaiemyekeh: Experiment, Investigation, Validation, Writing – review editing.

Haoyang Li: Experiment, Software, Investigation, Validation, Resources, Writing – review editing, Guidance.

James Hogan: Resources, Writing – review editing, Guidance, Supervision.

8. Acknowledgment

This work is supported by Defence Research and Development Canada (DRDC) through Natural Sciences and Engineering Research Council of Canada (NSERC) Collaborative Research and Development Grant - Department of National Defence (CRD-DND) project DNDPJ 531130-18 and by Defence Research and Development Canada (DRDC) General Dynamics Land Systems–Canada through NSERC Alliance project ALLRP 560447-2020. The views and conclusions contained in this document are those of the authors and should not be interpreted as representing the official policies, either expressed or implied, of General Dynamics, DRDC or the Government of Canada. The Government of Canada is authorized to reproduce and distribute reprints for Government purposes notwithstanding any copyright notation herein.

References

[1] J. J. Swab, Recommendations for determining the hardness of armor ceramics, International Journal of Applied Ceramic Technology 1 (3) (2004) 219–225.

[2] M. Anglada, Assessment of mechanical properties of ceramic materials, in: Advances in Ceramic Biomaterials, Elsevier, 2017, pp. 83–109.

[3] L. A. Hanner, J. J. Pittari III, J. J. Swab, Dynamic hardness of cemented tungsten carbides, International Journal of Refractory Metals and Hard Materials 75 (2018) 294–298.

[4] S. Yang, S. Yang, Y. Zhu, L. Fan, M. Zhang, Flash sintering of dense alumina ceramic discs with high hardness, Journal of the European Ceramic Society 42 (1) (2022) 202–206.

[5] E. Medvedovski, Ballistic performance of armour ceramics: Influence of design and structure. part 1, Ceramics International 36 (7) (2010) 2103–2115.

[6] C. Lo, H. Li, G. Toussaint, J. D. Hogan, On the evaluation of mechanical properties and ballistic performance of two variants of boron carbide, International Journal of Impact Engineering 152 (2021) 103846.

[7] J. J. Swab, J. J. Pittari III, W. R. Gamble, Uniaxial tensile strength and fracture analysis of a hot-pressed boron carbide, Journal of the European Ceramic Society 39 (6) (2019) 1965–1973.

[8] L. Zhang, D. Townsend, N. Petrinic, A. Pellegrino, Loading mode and lateral confinement dependent dynamic fracture of a glass ceramic macor, Journal of Dynamic Behavior of Materials (2022) 1–18.

[9] J. D. Hogan, L. Farbaniec, T. Sano, M. Shaeffer, K. Ramesh, The effects of defects on the uniaxial compressive strength and failure of an advanced ceramic, Acta Materialia 102 (2016) 263–272.

[10] J. D. Hogan, L. Farbaniec, N. Daphalapurkar, K. Ramesh, On compressive brittle fragmentation, Journal of the American Ceramic Society 99 (6) (2016) 2159–2169.

[11] Z. Wang, R. Li, W. Song, Dynamic failure and inelastic deformation behavior of sic ceramic under uniaxial compression, Ceramics International 46 (1) (2020) 612–617.

[12] J. Swab, W. Chen, J. Hogan, H. Liao, C. Lo, S. Mates, C. Meredith, J. Pittari, R. Rhorer, G. Quinn, Dynamic compression strength of ceramics: What was learned from an interlaboratory round robin exercise?, Journal of Dynamic Behavior of Materials 7 (1) (2021) 34–47.

[13] Y. Xu, F. Dai, Dynamic response and failure mechanism of brittle rocks under combined compression-shear loading experiments, Rock Mechanics and Rock Engineering 51 (3) (2018) 747–764.

[14] M. Shafiq, G. Subhash, An extended mohr–coulomb model for fracture strength of intact brittle materials under ultrahigh pressures, Journal of the American Ceramic Society 99 (2) (2016) 627–630.

[15] J. Lankford, C. Anderson Jr, G. Johnson, T. Holmquist, Dynamic compressive failure of ceramics under confinement, in: Proceedings of the 1991 Combat Vehicle Survivability Conference, Vol. 2, 1991, pp. 15–17.

[16] C. E. Anderson, P. E. O'Donoghue, J. Lankford, J. D. Walker, Numerical simulations of shpb experiments for the dynamic compressive strength and failure of ceramics, International journal of fracture 55 (3) (1992) 193–208.

[17] J. D. Hogan, L. Farbaniec, M. Shaeffer, K. Ramesh, The effects of microstructure and confinement on the compressive fragmentation of an advanced ceramic, Journal of the American Ceramic Society 98 (3) (2015) 902–912.

[18] L. Farbaniec, J. Hogan, K. Xie, M. Shaeffer, K. Hemker, K. Ramesh, Damage evolution of hot-pressed boron carbide under confined dynamic compression, International Journal of Impact Engineering 99 (2017) 75–84.

[19] Z. P. Bažant, F. C. Caner, Comminution of solids caused by kinetic energy of high shear strain rate, with implications for impact, shock, and shale fracturing, Proceedings of the National Academy of Sciences 110 (48) (2013) 19291–19294.

[20] F. C. Caner, Z. P. Bažant, Impact comminution of solids due to local kinetic energy of high shear strain rate: Ii–microplane model and verification, Journal of the Mechanics and Physics of Solids 64 (2014) 236–248.

[21] R. Clifton, An analysis of combined longitudinal and torsional plastic waves in a thin-walled tube, Tech. rep., Brown Univ Providence Ri Div of Engineering (1966).

[22] W. E. Baker, C. Yew, Strain-rate effects in the propagation of torsional plastic waves (1966).

[23] J. Duffy, J. Campbell, R. Hawley, On the use of a torsional split hopkinson bar to study rate effects in 1100-0 aluminum (1971).

[24] W. Zheng, S. Xu, C. Cai, S. Hu, A study of dynamic combined compression-shear loading technique based on hopkinson pressure bar, Chin J Theor Appl Mech 44 (1) (2012) 124–31.

[25] S. Xu, J. Huang, P. Wang, C. Zhang, L. Zhou, S. Hu, Investigation of rock material under combined compression and shear dynamic loading: an experimental technique, International Journal of Impact Engineering 86 (2015) 206–222.

[26] L. Zhou, S. Xu, J. Shan, Y. Liu, P. Wang, Heterogeneity in deformation of granite under dynamic combined compression/shear loading, Mechanics of Materials 123 (2018) 1–18.

[27] S. Tan, X. Yao, S. Long, X. Zhang, S. Zang, Static and dynamic strength of soda-lime glass under combined compression-shear loading, Journal of Non-Crystalline Solids 516 (2019) 14–25.

[28] D. Rittel, S. Lee, G. Ravichandran, A shear-compression specimen for large strain testing, Experimental Mechanics 42 (1) (2002) 58–64.

[29] J. Zhao, W. Knauss, G. Ravichandran, A new shear-compression-specimen for determining quasistatic and dynamic polymer properties, Experimental mechanics 49 (3) (2009) 427.

[30] S. P. Timoshenko, J. N. Goodier, Theory of elasticity (1951).

[31] W. W. Chen, B. Song, Split Hopkinson (Kolsky) bar: design, testing and applications, Springer Science & Business Media, 2010.

[32] H. Du, F. Dai, M. Wei, A. Li, Z. Yan, Dynamic compression–shear response and failure criterion of rocks with hydrostatic confining pressure: an experimental investigation, Rock Mechanics and Rock Engineering 54 (2) (2021) 955–971.

[33] B. M. Koch, P. Jannotti, D. Mallick, B. Schuster, T. Sano, J. D. Hogan, Influence of microstructure on the impact failure of alumina, Materials Science and Engineering: A 770 (2020) 138549.

[34] C. Lo, T. Sano, J. D. Hogan, Microstructural and mechanical characterization of variability in porous advanced ceramics using x-ray computed tomography and digital image correlation, Materials Characterization 158 (2019) 109929.

[35] T. Jiao, Y. Li, K. Ramesh, A. Wereszczat, High rate response and dynamic failure of structural ceramics, International Journal of applied ceramic technology 1 (3) (2004) 243–253.

[36] J. Lankford, W. Predebon, J. Staehler, G. Subhash, B. Pletka, C. Anderson, The role of plasticity as a limiting factor in the compressive failure of high strength ceramics, Mechanics of Materials 29 (3-4) (1998) 205–218.

[37] Z. Wang, P. Li, Dynamic failure and fracture mechanism in alumina ceramics: Experimental observations and finite element modelling, Ceramics International 41 (10) (2015) 12763–12772.

[38] J. Lankford, Mechanisms responsible for strain-rate-dependent compressive strength in ceramic materials, Journal of the American Ceramic Society 64 (2) (1981) C–33.

[39] J. Staehler, W. Predebon, B. Pletka, G. Subhash, Micromechanisms of deformation in high-purity hot-pressed alumina, Materials Science and Engineering: A 291 (1-2) (2000) 37–45.

[40] M. DeVries, G. Subhash, A. Mcghee, P. Ifju, T. Jones, J. Zheng, V. Halls, Quasi-static and dynamic response of 3d-printed alumina, Journal of the European Ceramic Society 38 (9) (2018) 3305–3316.

[41] G. Ravichandran, G. Subhash, Critical appraisal of limiting strain rates for compression testing of ceramics in a split hopkinson pressure bar, Journal of the American Ceramic Society 77 (1) (1994) 263–267.

[42] H. Li, P. Motamedi, J. Hogan, Characterization and mechanical testing on novel (γ+ α2)–tial/ti3al/al2o3 cermet, Materials Science and Engineering: A 750 (2019) 152–163.

[43] B. M. Koch, C. Lo, H. Li, T. Sano, J. Ligda, J. D. Hogan, Dynamic mechanical response of damaged alumina ad995, Journal of the European Ceramic Society 41 (3) (2021) 2034–2048.

[44] C. Lo, T. Sano, J. D. Hogan, Deformation mechanisms and evolution of mechanical properties in damaged advanced ceramics, Journal of the European Ceramic Society 40 (8) (2020) 3129–3139.

[45] K. Ramesh, G. Ravichandran, Dynamic behavior of a boron carbide aluminum cermet: experiments and observations, Mechanics of Materials 10 (1-2) (1990) 19–29.

[46] W. Chen, G. Ravichandran, Dynamic compressive failure of a glass ceramic under lateral confinement, Journal of the Mechanics and Physics of Solids 45 (8) (1997) 1303–1328.

[47] D. J. Frew, M. J. Forrestal, W. Chen, Pulse shaping techniques for testing brittle materials with a split hopkinson pressure bar, Experimental mechanics 42 (1) (2002) 93–106.

[48] B. M. Koch, C. Lo, H. Li, T. Sano, J. Ligda, J. D. Hogan, Two-dimensional dynamic damage accumulation in engineered brittle materials, Engineering Fracture Mechanics 244 (2021) 107539.

[49] B. Paliwal, K. Ramesh, An interacting micro-crack damage model for failure of brittle materials under compression, Journal of the Mechanics and Physics of Solids 56 (3) (2008) 896–923.

[50] C. Huang, G. Subhash, S. J. Vitton, A dynamic damage growth model for uniaxial compressive response of rock aggregates, Mechanics of materials 34 (5) (2002) 267–277.

[51] J. H. Yoo, J. C. Nam, S. Baik, Quantitative evaluation of glass-forming impurities in alumina: Equivalent silica concentration (esc), Journal of the American Ceramic Society 82 (8) (1999) 2233–2238.

[52] S. Stock, Recent advances in x-ray microtomography applied to materials, International materials reviews 53 (3) (2008) 129–181.

[53] S. I. Bae, S. Baik, Determination of critical concentrations of silica and/or calcia for abnormal grain growth in alumina, Journal of the American ceramic society 76 (4) (1993) 1065–1067.

[54] R. Landingham, A. Casey, Final report of the light armor materials program, Tech. rep., California Univ. (1972).

[55] F. Knudsen, Dependence of mechanical strength of brittle polycrystalline specimens on porosity and grain size, Journal of the American Ceramic Society 42 (8) (1959) 376–387.

[56] S. Nemat-Nasser, M. Obata, A microcrack model of dilatancy in brittle materials (1988).

[57] D. E. Grady, M. E. Kipp, Continuum modelling of explosive fracture in oil shale, in: International Journal of Rock Mechanics and Mining Sciences & Geomechanics Abstracts, Vol. 17, Elsevier, 1980, pp. 147–157.

[58] E. Eberhardt, D. Stead, B. Stimpson, Quantifying progressive pre-peak brittle fracture damage in rock during uniaxial compression, International Journal of Rock Mechanics and Mining Sciences 36 (3) (1999) 361–380.

[59] D. Warner, J. Molinari, Micromechanical finite element modeling of compressive fracture in confined alumina ceramic, Acta Materialia 54 (19) (2006) 5135–5145.

[60] S. Nemat-Nasser, H. Horii, Rock failure in compression, International Journal of Engineering Science 22 (8-10) (1984) 999–1011.

[61] H. Horii, S. Nemat-Nasser, Compression-induced microcrack growth in brittle solids: Axial splitting and shear failure, Journal of Geophysical Research: Solid Earth 90 (B4) (1985) 3105–3125.

[62] J. F. Shao, J. W. Rudnicki, A microcrack-based continuous damage model for brittle geomaterials, Mechanics of Materials 32 (10) (2000) 607–619.

[63] T. Sano, L. Vargas-Gonzalez, J. LaSalvia, J. D. Hogan, Dynamic failure and fragmentation of a hot-pressed boron carbide, Journal of Dynamic Behavior of Materials 3 (4) (2017) 548–556.

[64] G. Toussaint, I. Polyzois, Steel spheres impact on alumina ceramic tiles: Experiments and finite element simulations, International Journal of Applied Ceramic Technology 16 (6) (2019) 2131–2152.

[65] A. Bhattacharjee, A. Bhaduri, R. C. Hurley, L. Graham-Brady, Failure modeling and sensitivity analysis of ceramics under impact, Journal of Applied Mechanics 88 (5) (2021) 051007.

[66] M. Cil, Q. Zeng, R. Hurley, L. Graham-Brady, An integrative model for the dynamic behavior of brittle materials based on microcracking and breakage mechanics, Journal of Dynamic Behavior of Materials 6 (4) (2020) 472–488.

List of Figures